Computers & Graphics (2018)

Contents lists available at ScienceDirect

Computers & Graphics

journal homepage: www.elsevier.com/locate/cag

Constraint-based Point Set Denoising using Normal Voting Tensor and Restricted Quadratic Error Metrics

ARTICLE INFO

Article history:

Keywords: Point Set Denoising, Normal Voting Tensor, Binary Eigenvalues Optimization, Quadratic Error Metric

ABSTRACT

In many applications, point set surfaces are acquired by 3D scanners. During this acquisition process, noise and outliers are inevitable. For a high fidelity surface reconstruction from a noisy point set, a feature preserving point set denoising operation has to be performed to remove noise and outliers from the input point set. To suppress these undesired components while preserving features, we introduce an anisotropic point set denoising algorithm in the normal voting tensor framework. The proposed method consists of three different stages that are iteratively applied to the input: in the first stage, noisy vertex normals, are initially computed using principal component analysis, are processed using a vertex-based normal voting tensor and binary eigenvalues optimization. In the second stage, feature points are categorized into corners, edges, and surface patches using a weighted covariance matrix, which is computed based on the processed vertex normals. In the last stage, vertex positions are updated according to the processed vertex normals using restricted quadratic error metrics. For the vertex updates, we add different constraints to the quadratic error metric based on feature (edges and corners) and non-feature (planar) vertices. Finally, we show our method to be robust and comparable to state-of-the-art methods in several experiments.

1. Introduction

Point sets arise naturally in almost all kinds of three-dimensional acquisition processes, like 3D scanning. As early as 1985, they have been recognized as fundamental shape representations in computer graphics, [1]. Thus, they have manifold applications e.g. in face recognition ([2]), traffic accident analysis ([3]), or archeology ([4]).

However, during the acquisition process, due to mechanical limitations and surrounding conditions, noise and outliers are inevitably added to the point set. These artifacts have to be removed in a post-processing step to obtain a cleaned point set, which can be used in further steps like surface reconstruction, computer aided design (CAD), or 3D printing. There exists a variety of denoising methods focused on removing outliers and noise from the input point set to create a high fidelity output. These methods do not only aim at removing the undesired components, but also try to preserve sharp features of the geometry. High frequency components like corners or edges should be preserved and not be smoothed out. This is a challenging task as both features and noise are high frequency components and thus ambiguous in their nature.

Most state-of-the-art denoising methods are designed to work on triangle meshes. Compared to this setup, working on point sets and preserving sharp features is more difficult as explicit connectivity information is not present. Also, we assume the input to be given without any normals. However, as point sets take up less storage space and as the surface reconstruction is easier on a noise-free point set, we aim for an intrinsic smoothing method to work directly on the noisy point set input.

Our method is focused on the preservation of sharp features while removing noise and outliers from an input point set. The proposed algorithm follows an iterative three-step point set denoising scheme. (1) Noisy vertex normals processing using a vertex-based *normal voting tensor* (NVT) and *binary eigenvalues optimization* (BEO) similar to [5]. (2) Feature points de-

tection using an anisotropic covariance matrix. For the update of vertex positions, we use (3) a variation of the quadratic error norm adjusted to different kinds of feature points. Steps (1) to (3) are iteratively applied until a satisfactory output has been generated.

1.1. Related Work

1.1.1. Point-based Methods

In general, point sets appear as natural output of 3D scan devices. The increase in computational costs while processing polygonal meshes with growing size is partly responsible that points got recognized as primitives for surface representation, cf. [6]. One major drawback in this approach is the absence of connectivity information, which sets the task to declare surface normals. Here, [6] especially proposes a definition utilizing surfels, which are points equipped with normals. Usually point clouds do not carry normals, so we have to rely on methods which determine these robustly and with high quality. The authors Mitra and Nguyen [7] suggest a calculation of point set normals and an analysis under consideration of density, neighborhood sizes, and the presence of noise.

We are interested in point set denoising coupled with feature preservation. There are several works approaching these two properties directly. A first one was published by Fleishman et al. [8] – serving as a representative despite the fact that it deals with meshes instead of point clouds. As it does not use the mesh information, so it can be transferred to the point set setting. They use a bilateral filtering of points in normal direction in local neighborhoods. Another one is the anisotropic smoothing of point sets ([9]), where the authors use an anisotropic geometric curvature flow. Besides the high dependency on suitable neighborhoods, which the authors cannot compute directly, the proposed algorithm does not detect features explicitly, but incorporates feature detection into an anisotropic Laplacian. The more recent work [10] is based on the idea of sparsity methods and includes L_0 minimization. Originating from image denoising, they set up an energy consisting of the 3D signal to be optimized coupled with an L_0 optimization applied to a differential operator on the signal.

Processing of normals, point positions, and an edge-aware upsampling offers the opportunity for an iterative application. In this setting, we are going to compare our algorithm with that of [11], called "moving robust principal component analysis" (MRPCA). The idea is – like the previous – based on sparsity methods, which takes sparsity-algorithms and adapt them to geometry processing problems. They perceive the point cloud as a collection of overlapping two-dimensional subspaces and do not rely – in contrast to other procedures – on oriented normals as input. The method is robust against outliers and capable of denoising the point cloud while handling sharp features.

Recently, Zheng et al. ([12]) proposed an extension of edge-aware image processing and mesh denoising to point clouds. In their four-staged approach, feature candidates are detected, employing a feature structure by the l_1-medial skeleton, calculating and equipping these with multiple normals, and selecting guiding normals by using kNN patches with its normals being most consistent. In this terms, the algorithm is even capable of high intensive noise while preserving important geometric features.

1.1.2. Surface Reconstruction with Feature Preservation

One of the processes most affected by noise and outliers in a point set is that of surface reconstruction. A thorough introduction is given in the survey [13]. All following techniques aim at preserving features while simultaneously perform denoising in the surface reconstruction process. In the context of local smoothness priors, the moving least squares (MLS) approach has a major impact. Developed in large parts by Levin [14], MLS underwent a lot of modifications. Guennebaud et al. [15] modified the MLS idea by replacing the concept of finding well-defined tangent planes by fitting spheres as higher order approximations to the surface. This change makes the method more robust – especially in sparsely sampled regions, where a well defined tangent plane might not exist. Their method is denoted as "algebraic point set surfaces" (APSS) and will serve as comparison to our algorithm. The method of Öztireli et al. [16] aims at overcoming the sensitivity of MLS to outliers and the effect of smoothing out small or sharp features. They combine MLS with local kernel regression to create a new implicit description of the surface, making it robust to noise, outliers, and even sparse sampling. Their method of "robust implicit moving least squares" (RIMLS) will be the third algorithm we compare to. More recently, Chen et al. [17] set their focus on a new MLS formalism using higher-order approximations – like APSS – incorporating discrete non-oriented gradient fields, yielding a continuous implicit representation.

Turning to hierarchical partitioning, Ohtake et al. [18] propose "multi-level partitioning of unity implicits" (MPU). Their technique consists of an octree-based top-down structure, where points in a cell and nearby are approximated by either a bivariate quadratic polynomial or an algebraic trivariate quadric. An adjustment parameter for the level of smoothness guarantees the handling of noise with respect to an error residual tolerance.

Considering piecewise smooth priors and partition based methods, Fleishman et al. [19] concentrate with their robust moving least squares (RMLS) on the handling of sharp features. They use the robust statistics tool of forward-search paradigm to choose small sets of points excluding outliers, continuing through the cloud, and evaluating observations monitored by statistical estimates. Wang et al. [20] robustly compute a feature preserving normal field by mean-shift clustering and a least median of squares (LMS) regression scheme, providing local partitions, to which edge-preserving smoothing is applied by fitting multiple quadrics. Due to the locality, feature fragmentation at sharp edges may occur.

Taking sparsity and neighboring normals into account, Avron et al. [21] use global L_1 optimization on these normals, observing that differences between them should be sparse, yet large values should reflect sharp features. Similar to the approach in RIMLS, [22] suggests the edge-aware resampling (EAR) of the point cloud. This is a feature-sensitive method under the guidance of the locally optimal projection (LOP) ([23]) in a two-staged approach, starting their robust smoothing and re-

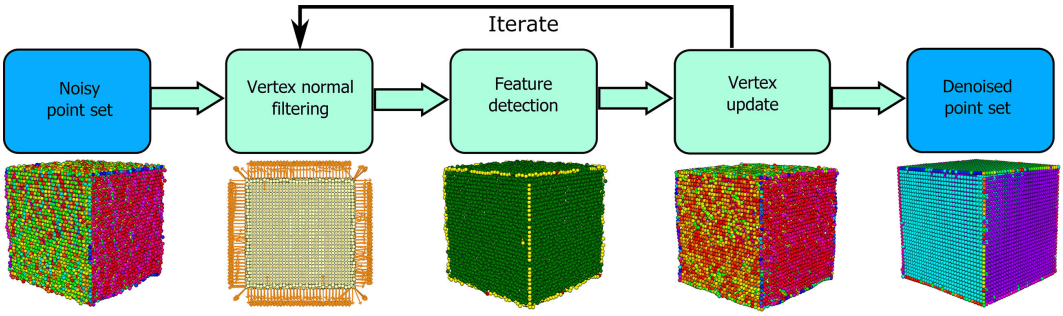

Fig. 1: The pipeline of the proposed algorithm. Our method consists of three different stages, which are iterated until a desired output is produced.

sampling process in regions with similar normal distribution, while approaching the edges in terms of both smoothing and resampling in a second step.

1.2. Contribution

On a noisy point set, it is a challenging task to decouple noise components and sharp features, which is essential for a noise-free point set reconstruction. As shown in Figure 1, our algorithm consists of three different stages, which are iteratively applied until a satisfactory output has been computed. In the first stage, which is vertex normal filtering, we extend the concept of face normal processing of Yadav et al. [5] to the more general setup of vertex normal processing. Although our vertex normal processing is similar to the face normal processing of Yadav et al. [5], we define a vertex-based *Normal Voting Tensor* (NVT) based on the variation of vertex normals. In terms of noise sensitivity, vertex normals are more sensitive compared to face normals. Therefore, we modify the weighting scheme in the neighborhood selection to make the algorithm robust against different levels of noise. Noise and sharp features are decoupled using the spectral analysis of the vertex-based NVT and noise components are suppressed using *Binary Eigenvalues Optimization* (BEO). In the second stage, we introduce an anisotropic covariance matrix using the filtered vertex normals to detect feature points (edges and corners) robustly on the noisy input point set. In the last stage, we update the vertex positions based on quadratic error metrics. A corresponding quadratic error metric is used based on different feature points. The proposed vertex update method helps the algorithm to preserve sharp features with minimum shrinkage during the denoising process.

2. Method

Let us consider a nonuniform and noisy input point set $\mathbf{V} = \{\mathbf{v}_0, \mathbf{v}_1, \cdots, \mathbf{v}_{n-1}\} \subset \mathbb{R}^3$ sampling a surface with $n \in \mathbb{N}$ denoting the number of vertices. We assume these data points to be acquired e.g. by a 3D laser scanner and not to be equipped with vertex normals. Thus, a first normal field on the vertices is computed following [24], which results in consistently oriented normals. Despite the fact, that there are more recent works dealing with consistent normal fields on point sets, we decided to use [24], as the implementation is simple and it works well with all the models we used for our experiments. This is mostly due to the fact, that we process and smooth the normals further, so a consistent initial normal field is sufficient for our purposes. We denote the normal at vertex $\mathbf{v}_i$ by $\mathbf{n}_i$ and the normal field by $\mathbf{N} = \{\mathbf{n}_0, \mathbf{n}_1, \cdots, \mathbf{n}_{n-1}\} \subset \mathbb{R}^3$. For a given vertex $\mathbf{v}_i$, we denote by $\mathbf{\Omega}_i := \{j \in \mathbb{N} \mid \mathbf{v}_j \in \mathbf{V} \cap B_r(\mathbf{v}_i), i \neq j, j < n\}$, a set of indices of the geometric neighborhood of vertex $\mathbf{v}_i$, i.e. indices of all points from $\mathbf{V}$ that have distance less or equal r to $\mathbf{v}_i$, where r is a global parameter. We favor a geometric neighborhood over a combinatorial k-nearest neighborhood as [5] found it to be more robust. In the following, we will denote by $\tilde{\cdot}$ those elements updated in one iteration, which will then serve as input to the next one.

2.1. Vertex Normal Filtering

This is the first of three iteratively applied steps of the proposed method. Here, noisy vertex normals are filtered and denoised using a vertex-based *Normal Voting Tensor* (NVT) and *Binary Eigenvalues Optimization* (BEO) similar to [5]. We describe both in the following.

2.1.1. Vertex-based Normal Voting Tensor (NVT)

Covariance matrices compute the variance of an entity in a well defined domain. For example, consider a vertex $\mathbf{v}_i$ and its nearest neighbors $\mathbf{v}_j$, $j \in \mathbf{\Omega}_i$. The covariance matrix on the edges $\mathbf{v}_j - \mathbf{v}_i$ of the nearest neighbor graph computes the variance of the vertex $\mathbf{v}_i$ in $\mathbb{R}^3$. Similarly, the covariance matrix of vertex normals $\mathbf{n}_j$, $j \in \mathbf{\Omega}_i$ in a well defined neighborhood computes the anisotropic nature of a point set in that region. To analyze the anisotropic nature of a shape – in this case a point set surface – we define an object related to the covariance matrix, namely the vertex-based NVT, which is computed using the neighboring vertex normals:

$$\mathbf{T}_i = \frac{1}{\sum_{j \in \mathbf{\Omega}_i} w_{ij}} \sum_{j \in \mathbf{\Omega}_i} w_{ij}\, \mathbf{n}_j \otimes \mathbf{n}_j, \tag{1}$$

where $\mathbf{\Omega}_i$ is the geometric neighborhood centered at $\mathbf{v}_i$ and the symbol $\otimes$ represents the outer product $\mathbf{n}_j \mathbf{n}_j^T$. The weights w_{ij} are computed based on the similarity between the neighbor normals. To define w_{ij}, we follow the local binary neighborhood concept, where the central vertex normal $\mathbf{n}_i$ is compared to neighborhood vertex normals $\mathbf{n}_j$ and assigns a binary value $\omega_{ij} \in \{0, 1\}$ according to the normal difference. Formally, we define the weight term w_{ij} as

$$w_{ij} = \begin{cases} 1 & \text{if } \angle(\mathbf{n}_i, \mathbf{n}_j) \leq \rho \\ 0 & \text{if } \angle(\mathbf{n}_i, \mathbf{n}_j) > \rho, \end{cases} \tag{2}$$

where $\rho \in \mathbb{R}_{>0}$ is given by the user and denotes a local binary neighborhood threshold, which is used to select vertices $\mathbf{v}_j$, $j \in \mathbf{\Omega}_i$ with similar normals to $\mathbf{n}_i$. The weight term w_{ij} is not the exact weight function used in [5] because vertex normals are more sensitive to noise than face normals, for example at sharp features. Therefore, a harder cut-off is necessary to maintain geometrical features while smoothing the point set. Figure 2 shows a comparison between the proposed weighting scheme (2), the bilateral weighting from [25], and the weighting function used in Yadav et al. [5]. As it can be seen, the harder cut-off function is more effective in terms of feature preservation than Yadav et al. [5] or [25].

The term $\mathbf{T}_i$ is a tensor. By construction, it is symmetric and positive semidefinite and can be represented in terms of its spectral components:

$$\mathbf{T}_i = \sum_{\ell=1}^{3} \lambda_{i,\ell}\, \mathbf{x}_{i,\ell} \otimes \mathbf{x}_{i,\ell}, \tag{3}$$

where $\lambda_{i,\ell}$ and $\mathbf{x}_{i,\ell}$ are the corresponding eigenvalues and eigenvectors. Let us consider the eigenvalues to be sorted in decreasing order $\{\lambda_{i,1} \geq \lambda_{i,2} \geq \lambda_{i,3} \geq 0\}$. Thus, we can rewrite $\mathbf{T}_i$ as:

$$\begin{aligned}\mathbf{T}_i =&(\lambda_{i,1} - \lambda_{i,2})\mathbf{x}_{i,1} \otimes \mathbf{x}_{i,1} + (\lambda_{i,2} - \lambda_{i,3})(\mathbf{x}_{i,1} \otimes \mathbf{x}_{i,1} + \mathbf{x}_{i,2} \otimes \mathbf{x}_{i,2}) \\ &+ \lambda_{i,3}(\mathbf{x}_{i,1} \otimes \mathbf{x}_{i,1} + \mathbf{x}_{i,2} \otimes \mathbf{x}_{i,2} + \mathbf{x}_{i,3} \otimes \mathbf{x}_{i,3}).\end{aligned} \tag{4}$$

Here, the first term of the right hand side is known as the stick tensor and has only one dominant eigenvalue in the normal direction. The second term is spanned by the two dominant eigenvectors, such that the normal direction is defined in the direction of the least dominant eigenvector. This term is known as the plate tensor. The third term is spanned by all eigenvectors and does not have a well defined normal direction, cf. [26]. From the above description, it is clear that the vertex-based NVT captures the anisotropic nature of a point set and feature points can be easily detected using the eigenvalues of $\mathbf{T}_i$. That is, if there is only one dominant eigenvalue then it is a planar point, if two eigenvalues are dominant then it is an edge, and if all eigenvalues are equally dominant then it is a corner.

2.1.2. Binary Eigenvalues Optimization (BEO)

In our method, the vertex-based NVT is applied as a denoising operator on a noisy point set. Furthermore, as we have discussed in the last section, the vertex-based NVT is capable of detecting features on point sets as shown in Figure 1 (third column). However, on a noisy point set, the behavior of the spectral components of the vertex-based NVT will change.

Let us assume that a point set is corrupted by random noise with standard deviation σ_n. Due to the presence of noise, the eigenvalues of the vertex-based NVT will change. For example, on a planar area, one eigenvalue will remain dominant, but the other two eigenvalues will be non-zero and proportional to σ. Similarly, on an edge of the sampled geometry, the least dominant eigenvalue will be proportional to the applied noise, i.e. $\lambda_{i,3} \propto \sigma$. On a corner of the sampled geometry we expect $\lambda_{i,1}, \lambda_{i,2}, \lambda_{i,3} \gg \sigma$. To remove these noise effects from the vertex-based NVT, the eigenvalues of $\mathbf{T}_i$ should be modified. That is, on a planar area and on an edge the least dominant eigenvalues should be zero and at a corner all eigenvalues should be equally dominant. In order to achieve this, we turn to binary optimization.

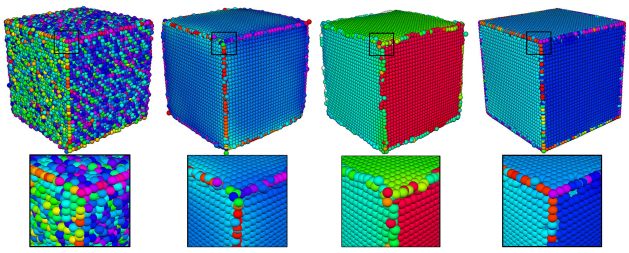

(a) $\sigma_n = 0.25\ell_a$ (b) w_{ij} as in [5] (c) Bilateral [25] (d) As in Eq. 2

Fig. 2: A comparison between different weighting functions for neighborhood selection. (a) The cube model is corrupted with a Gaussian noise ($\sigma_n = 0.25\ell_a$) in random directions, where l_a is the average distance between vertices of the point set. (b) The output obtained by using the weighting function mentioned in Yadav et al. [5]. (c) The output obtained by using the bilateral weighting function (smooth functions) mentioned in Yadav et al. [25]. (d) The output obtained by using the proposed weighting function of Equation (2). Vertices of the cube are colored based on the variation of vertex normals. We computed the scalar product between the normal of a random vertex and rest of the vertex normals to show the level of denoising and feature preservation.

The concept of binary eigenvalues optimization is applied to the eigenvalues of $\mathbf{T}_i$, where each eigenvalue will be assigned a binary value $\tilde{\lambda}_{i,\ell} \in \{0, 1\}$ to remove noise components effectively. Similar to [5], a threshold value $\tau \in \mathbb{R}_{>0}$ is used for the BEO. The term τ is a global parameter given by the user and should be chosen according to the noise intensity, i.e. $\tau \propto \sigma$, and to be smaller than the dominant eigenvalue(s). We will denote by $\tilde{\lambda}_{i,\ell}$ the modified eigenvalues of the vertex-based NVT after BEO. The modification is based on feature classification:

- At corners of the sampled geometry, when considering the point set, the smallest eigenvalue should still be bigger than the threshold value, i.e. $\lambda_{i,3} \geq \tau$. Hence, we set:

$$\tilde{\lambda}_{i,\ell} = 1, \quad \ell \in \{1, 2, 3\} \quad \text{if} \quad \lambda_{i,3} \geq \tau.$$

- At edges of the sampled geometry, in the noisy point set, the least dominant eigenvalue should be smaller than the threshold value, i.e. $\lambda_{i,3} < \tau$ and $\lambda_{i,2} \geq \tau$. Hence, we set:

$$\tilde{\lambda}_{i,1} = \tilde{\lambda}_{i,2} = 1, \quad \tilde{\lambda}_{i,3} = 0 \quad \text{if} \quad \lambda_{i,2} \geq \tau, \quad \lambda_{i,3} < \tau.$$

- In the last case, we check for planar areas of the geometry. Having $\lambda_{i,2} < \tau$ and $\lambda_{i,3} < \tau$ shows that the only dominant eigenvalue is $\lambda_{i,1}$. Hence, we set:

$$\tilde{\lambda}_{i,1} = 1, \quad \tilde{\lambda}_{i,2} = \tilde{\lambda}_{i,3} = 0 \quad \text{if} \quad \lambda_{i,1} \geq \tau, \quad \lambda_{i,3}, \lambda_{i,2} < \tau.$$

The BEO procedure presented here will remove the noise components from the eigenvalues of the vertex-based NVT.

2.1.3. Vertex Normal Denoising

To remove noise components from the vertex normals, we project the noisy vertex normals towards smooth normals by

multiplication of the vertex-based NVT to the corresponding vertex normal. By the preceding BEO, this multiplication procedure will suppress noise in weak eigendirections and will strengthen vertex normals in strong eigendirections.

Before multiplication, we have to recompute the modified vertex-based NVT by using the same eigenvectors with the eigenvalues optimized in the BEO:

$$\tilde{\mathbf{T}}_i = \sum_{\ell=1}^{3} \tilde{\lambda}_{i,\ell}\, \mathbf{x}_{i,\ell} \otimes \mathbf{x}_{i,\ell}. \tag{5}$$

To remove noise, we multiply the corresponding vertex normal with the modified tensor $\tilde{\mathbf{T}}_i$. The multiplication will lead to noise removal while retaining sharp features:

$$\tilde{\mathbf{n}}_i = d\mathbf{n}_i + \tilde{\mathbf{T}}_i\mathbf{n}_i = d\mathbf{n}_i + \sum_{\ell=1}^{3} \tilde{\lambda}_{i,\ell}\langle \mathbf{x}_{i,\ell}, \mathbf{n}_i\rangle \mathbf{x}_{i,\ell}, \tag{6}$$

where $d \in \mathbb{R}_{>0}$ denotes a damping factor to control the denoising speed of the vertex normals. We use $d = 3$ for all experiments. Finally, the updated normal $\tilde{\mathbf{n}}_i$ is normalized.

2.2. Feature Detection

This is the second of three iteratively applied steps of the proposed method. Here, we classify the point set into three different categories: corners, edges, and planar points. This will be done using the spectral analysis of a weighted covariance matrix. The idea to identify points and their features is substantiated in the follow-up treatment of point position updates in the upcoming third subsection where we use the notion of a quadratic error metric applied differently to the occurring feature-assigned points. The weighted covariance matrix is defined using filtered vertex normals, which makes the proposed algorithm more robust against feature points misclassification, which can lead to feature blurring artifacts.

To detect feature points on a point set with filtered vertex normals, we consider the weighted covariance matrix:

$$\mathbf{C}_i = \frac{1}{\sum_{j\in\mathbf{\Omega}_i} \tilde{w}_{ij}} \sum_{j\in\mathbf{\Omega}_i} \tilde{w}_{ij}(\mathbf{v}_j - \bar{\mathbf{v}}) \otimes (\mathbf{v}_j - \bar{\mathbf{v}}), \tag{7}$$

where the weights $\tilde{w}_{ij}$ are similar to Equation (2), but are now utilizing the filtered vertex normals of Section 2.1. Formally, the terms $\bar{\mathbf{v}}$ and $\tilde{w}_{ij}$ are defined as:

$$\bar{\mathbf{v}} = \frac{1}{\sum_{j\in\mathbf{\Omega}_i} \tilde{w}_{ij}} \sum_{j\in\mathbf{\Omega}_i} \tilde{w}_{ij}\mathbf{v}_j, \quad \tilde{w}_{ij} = \begin{cases} 1 & \text{if } \angle(\tilde{\mathbf{n}}_i, \tilde{\mathbf{n}}_j) \le \rho \\ 0 & \text{if } \angle(\tilde{\mathbf{n}}_i, \tilde{\mathbf{n}}_j) > \rho \end{cases}. \tag{8}$$

Similar to the vertex-based NVT, $\mathbf{C}_i$ is also a symmetric and positive semidefinite matrix and can be represented in terms of its spectral components:

$$\mathbf{C}_i = \sum_{\ell=1}^{3} \mu_{i,\ell}\, \mathbf{y}_{i,\ell} \otimes \mathbf{y}_{i,\ell}, \tag{9}$$

where μ_ℓ and $\mathbf{y}_\ell$ are the corresponding eigenvalues and eigenvectors. Let us consider the eigenvalues to be sorted in decreasing order $\{\mu_{i,1} \ge \mu_{i,2} \ge \mu_{i,3} \ge 0\}$. In the proposed method, they are used to classify the points as follows, utilizing the same threshold parameter τ as in Section 2.1.2:

- On a planar area, there will be two dominant eigenvalues and their corresponding eigenvectors should be spanning the tangent plane. The least dominant eigenvalue will be smaller than the feature threshold τ. Therefore, we classify planar points as

$$\mathbf{V}_f = \{\mathbf{v}_i \in \mathbf{V} \mid \mu_{i,1}, \mu_{i,2} \ge \tau,\ \mu_{i,3} < \tau\}.$$

- On an edge, there will be one dominant eigenvalue and the corresponding eigenvector aligns with the edge direction. Therefore, we classify edge points as

$$\mathbf{V}_e = \{\mathbf{v}_i \in \mathbf{V} \mid \mu_{i,1} \ge \tau,\ \mu_{i,2}, \mu_{i,3} < \tau\}.$$

- Finally, on a corner, either all eigenvalues are dominant or none of them is significant. Therefore, corner points are set to

$$\mathbf{V}_c = \{\mathbf{v}_i \in \mathbf{V} \mid (\mu_{i,1}, \mu_{i,2}, \mu_{i,3} \ge \tau) \vee (\mu_{i,1}, \mu_{i,2}, \mu_{i,3} < \tau)\}.$$

Points at a corner, an edge, and planar points are represented in the following by $\mathbf{V}_c = \{\mathbf{v}_\cdot^c\}$, $\mathbf{V}_e = \{\mathbf{v}_\cdot^e\}$, and $\mathbf{V}_f = \{\mathbf{v}_\cdot^f\}$ respectively, such that we obtain the following disjoint union $\mathbf{V} = \mathbf{V}_c \sqcup \mathbf{V}_e \sqcup \mathbf{V}_f$.

2.3. Constraint-based Vertex Position Update

In this final of three iteratively applied steps of the proposed method, we update the vertex positions. This is done utilizing distance-based constraints, where the resulting updated point set remains within a prescribed distance to the input noisy point set. To compute the optimal position of a vertex w.r.t. the smoothed vertex normal, restricted quadratic error metrics are used in this algorithm, inspired by the work of [27]. The restriction to the quadratic error metric is introduced based on the different feature points and the vertex position is updated utilizing distance-based constraints.

We allow the user to provide a parameter $\varepsilon \in \mathbb{R}_{>0}$ bounding the maximum deviation d_i between an initial noisy point and its corresponding iteratively updated point $\tilde{\mathbf{v}}_i$.

2.3.1. Vertex Update at Corners

Let us consider a point $\mathbf{v}_i^c \in \mathbf{V}_c$, labeled as corner point in Section 2.2. We will find its updated position $\tilde{\mathbf{v}}_i^c$ by minimizing the following energy function:

$$\min_{\tilde{\mathbf{v}}_i^c} \sum_{j\in\mathbf{\Omega}_i} \|\tilde{\mathbf{n}}_j \cdot (\tilde{\mathbf{v}}_i^c - \mathbf{v}_j)\|^2. \tag{10}$$

Each of the neighboring vertices $\mathbf{v}_j$ is equipped with a corresponding filtered normal direction $\tilde{\mathbf{n}}_j$. Thus, we can associate a plane based at each neighboring vertex given by the normal direction. In an ideal case, these planes would all meet in a point – the exact position of the vertex $\mathbf{v}_i$. But as noise is present and the planes will in general not intersect in a point, we define the error of the vertex $\tilde{\mathbf{v}}_i^c$ as the sum of squared distances to these planes.

Note that we do not weight the neighbors in Equation (10), but take all $j \in \mathbf{\Omega}_i$ into account equally. That is because we

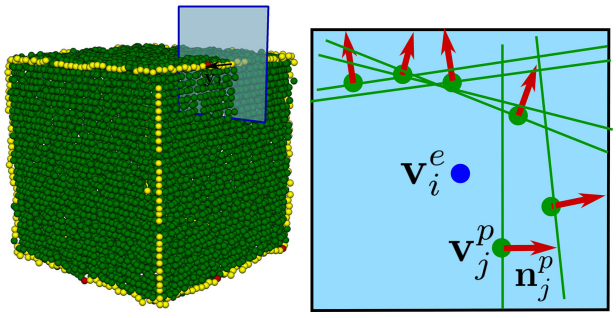

(a) (b)

Fig. 3: A visual representation of the vertex update scheme at edges. Figure (a) shows the plane $\mathbf{H}_i$, which is defined by $\mathbf{y}_1$ for edge vertex $\mathbf{v}_i^e$. Neighbor vertices of $\mathbf{v}_i^e$ and corresponding vertex normals are projected onto this plane as shown in Figure (b).

rely on the highly unstable intersection of multiple planes in $\mathbb{R}^3$. The more we take into account, the more likely it is for them to even out noise effects and give a faithful reconstruction of the corner.

Minimizing Equation (10) boils down to solving a linear system and the new position can be computed directly, which will be given by the following equation:

$$\mathbf{t}_i^c = \left(\sum_{j \in \mathbf{\Omega}_i} \tilde{\mathbf{n}}_j \otimes \tilde{\mathbf{n}}_j \right)^{-1} \sum_{j \in \mathbf{\Omega}_i} \left(\tilde{\mathbf{n}}_j \otimes \tilde{\mathbf{n}}_j \mathbf{v}_j \right),$$

where $\mathbf{t}_i^c$ is a temporary vertex position. Before updating the position of $\mathbf{v}_i^c$ to $\tilde{\mathbf{v}}_i^c$, we compute the deviation d_i between $\mathbf{t}_i^c$ and the corresponding original vertex from the noisy point set. If d_i is within the user-prescribed limit ε we move this corner point to $\mathbf{t}_i^c$, otherwise we don't move this point:

$$\tilde{\mathbf{v}}_i^c = \begin{cases} \mathbf{t}_i^c & \text{if } d_i \leq \varepsilon \\ \mathbf{v}_i^c & \text{if } d_i > \varepsilon \end{cases}, \tag{11}$$

where ε is the aforementioned user input which limits the deviation between the original noisy and updated corner points. By the above equation, corner points are moved at most ε during their position update in the direction of a minimum distance to all neighboring planes spanned by the respective normals.

2.3.2. *Vertex Update at Edges*

Let us consider a point $\mathbf{v}_i^e \in \mathbf{V}_e$, labeled as edge point in Section 2.2. Here, the weighted covariance matrix $\mathbf{C}_i$ has only one dominant eigenvalue $\mu_{i,1}$ and the corresponding eigenvector $\mathbf{y}_{i,1}$ aligns with the edge direction. We define a plane

$$\mathbf{H}_i = \{x \in \mathbb{R}^3 \mid \langle \mathbf{y}_{i,1}, x \rangle = \langle \mathbf{y}_{i,1}, \mathbf{v}_i^e \rangle\}.$$

As shown in Figure 3, we project all neighborhood vertices $\mathbf{v}_j$, $j \in \mathbf{\Omega}_i$ and their respective vertex normals $\tilde{\mathbf{n}}_j$ to $\mathbf{H}_i$, denoting the corresponding projections by $\mathbf{v}_j^\pi$ and $\tilde{\mathbf{n}}_j^\pi$:

$$\begin{aligned} \mathbf{v}_j^\pi &= \mathbf{v}_j - \langle (\mathbf{v}_j - \mathbf{v}_i^e), \mathbf{y}_{i,1} \rangle \mathbf{y}_{i,1}, \\ \tilde{\mathbf{n}}_j^\pi &= \tilde{\mathbf{n}}_j - \langle \tilde{\mathbf{n}}_j, \mathbf{y}_{i,1} \rangle \mathbf{y}_{i,1}. \end{aligned}$$

Now, we define a quadratic energy function similar to Equation (10):

$$\min_{\tilde{\mathbf{v}}_i^e} \sum_{j \in \mathbf{\Omega}_i} \left(\|\tilde{\mathbf{n}}_j^\pi \cdot (\tilde{\mathbf{v}}_i^e - \mathbf{v}_j^\pi)\|^2 + \frac{1}{|\mathbf{\Omega}_i|} \|\mathbf{y}_{i,1} \cdot (\tilde{\mathbf{v}}_i^e - \mathbf{v}_j^\pi)\|^2 \right). \tag{12}$$

The above energy function is defined on the plane $\mathbf{H}_i$. In comparison to Equation (10), we include an additional summand. This is necessary, because the matrix of the linear system resulting from Equation (12) without the summand would not be invertible. The reason is, that the least dominant eigenvalue along the normal being zero would reduce the rank of the corresponding matrix. We choose this additional summand which is directed along the edge to create an orthonormal basis as the plane $\mathbf{H}_i$ is spanned using the other two eigenvectors of the weighted covariance matrix $\mathbf{C}_i$. Including the summand, we can minimize Equation (12) once more by solving a linear system which results in the equation:

$$\mathbf{t}_i^e = \left(\sum_{j \in \mathbf{\Omega}_i} \tilde{\mathbf{n}}_j^\pi \otimes \tilde{\mathbf{n}}_j^\pi + \mathbf{y}_{i,1} \otimes \mathbf{y}_{i,1} \right)^{-1} \sum_{j \in \mathbf{\Omega}_i} \left(\tilde{\mathbf{n}}_j^\pi \otimes \tilde{\mathbf{n}}_j^\pi \mathbf{v}_j + \mathbf{y}_{i,1} \otimes \mathbf{y}_{i,1} \mathbf{v}_i^e \right),$$

where the summand $\mathbf{y}_1 \otimes \mathbf{y}_1$ ensures that the matrix is invertible. The term $\mathbf{t}_i^e$ is a temporary vertex position and we once more compute the deviation between $\mathbf{t}_i^e$ and the corresponding original vertex from the noisy point set to modify the edge vertex accordingly:

$$\tilde{\mathbf{v}}_i^e = \begin{cases} \mathbf{t}_i^e & \text{if } d_i \leq \varepsilon \\ \mathbf{v}_i^e & \text{if } d_i > \varepsilon \end{cases}. \tag{13}$$

For each edge vertex, the above equation computes the optimal position by minimizing the distance between the lines, which are defined by the projected vertex normals. This operation effectively preserves sharp features along edges and removes noise effectively.

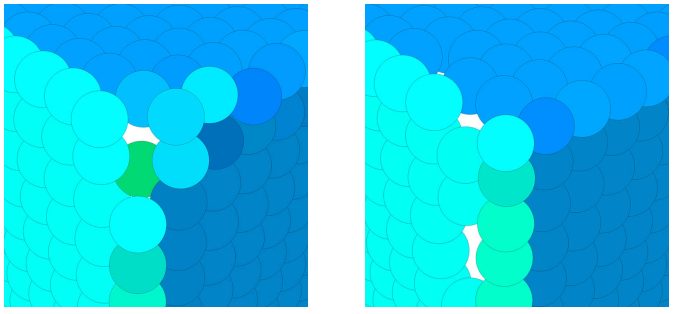

(a) (b)

Fig. 4: This figure shows the effect of the proposed constraint-based vertex position update scheme: Figure (a) represents the point set reconstructed by using Equation (14) not only for flat regions but also for feature points. Figure (b) represents the result obtained by the proposed scheme, where flat regions follow Equation (14), edges are reconstructed using Equation (13) and corner positions are updated using Equation (11). Note how the corner itself is not recovered in (a), but is recovered in (b).

2.3.3. *Vertex Update on Flat Regions*

Let us consider a point $\mathbf{v}_i^f \in \mathbf{V}_f$, labeled as point within a planar area by Section 2.2. In this flat region, the matrix $\mathbf{C}_i$ has

two dominant eigenvalues. In order to remove noise in these regions, we allow to move the vertex position only in direction of the corresponding vertex normal $\tilde{\mathbf{n}}_i$. Thereby, we follow the approach of [28, 29]. We use an energy function similar to that of Equation (10), but with the restriction to only move in normal direction. Similar to edge and corner vertex updates, we first compute the deviation d_i and then update the vertex position according to

$$\tilde{\mathbf{v}}_i^f = \begin{cases} \mathbf{v}_i^f + \frac{\alpha}{\sum_{j\in\mathbf{\Omega}_i} W_{ij}} \sum_{j\in\mathbf{\Omega}_i} W_{ij}\langle\tilde{\mathbf{n}}_j, \mathbf{v}_j - \mathbf{v}_i^f\rangle\tilde{\mathbf{n}}_i & \text{if} \quad d_i \le \varepsilon \\ \mathbf{v}_i^f & \text{if} \quad d_i > \varepsilon \end{cases}, \quad (14)$$

where α is a user-controlled parameter to limit the amount of smoothing on flat regions and W_{ij} is a combination of a similarity and a closeness function:

$$W_{ij} = \exp\Big(-\frac{16|\tilde{\mathbf{n}}_i - \tilde{\mathbf{n}}_j|^2}{\delta^2}\Big) \cdot \exp\Big(-\frac{4|\mathbf{v}_j - \mathbf{v}_i^f|^2}{\delta^2}\Big), \quad (15)$$

where δ is half the diameter of the point set $\mathbf{\Omega}_i$.

Even though the update scheme for flat regions as given in Equation (14) seems most elaborate, the combination with simpler schemes for both corners (11) and edges (13) is more effective in practice, as shown in Figure 4.

2.4. Method Summary

In the previous Sections 2.1, 2.2, and 2.3, we have presented the three key steps of our smoothing method. By iteratively applying these three steps to a noisy point set input, the proposed algorithm produces a noise-free point set with proper sharp features.

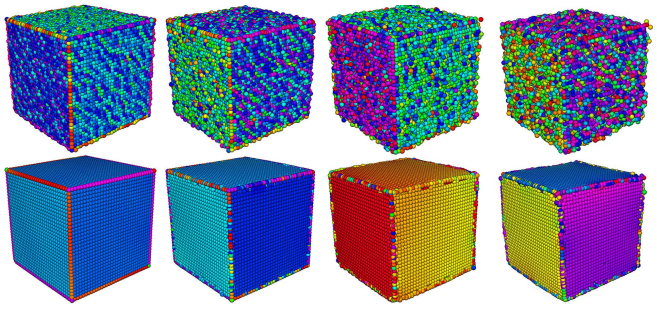

(a) $\sigma_n = 0.13l_a$ (b) $\sigma_n = 0.25l_a$ (c) $\sigma_n = 0.35l_a$ (d) $\sigma_n = 0.5l_a$

Fig. 5: A visual representation of feature preservation analysis. The Cube is corrupted with different levels of noise ($\sigma_n = 0.13l_a, 0.25l_a, 0.35l_a, 0.5l_a$) in random direction. To measure the feature preservation capability of the proposed algorithm, we computed MAD (mean angular deviation) and from Figure (a)-(d) MAD are 2.99, 4.15, 6.4 and 6.48. Vertices are colored based on the variation of vertex normals. We computed the scalar product between the normal of a random vertex and rest of the vertex normals to show the level of denoising.

3. Experiments, Results and Discussion

We evaluated the capacity of our algorithm on various kinds of point set models corrupted with synthetic noise (Figures 5, 6, 9, 10, 12) and real scanned data (Figures 13, 14). We compared our method with five state-of-the-art denoising Methods [11], [12], [15], [16], and [30]. Methods [15] and [16] are implemented in MeshLab. The results of Methods [11], [12], and [30] are provided by the authors.

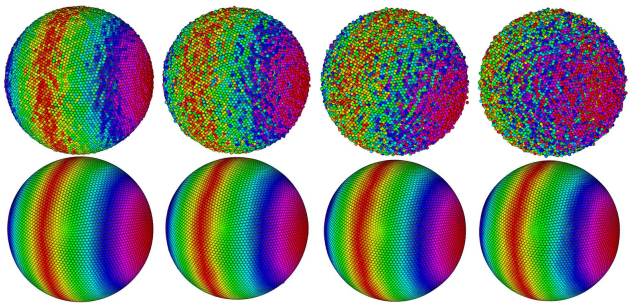

(a) $\sigma_n = 0.13l_a$ (b) $\sigma_n = 0.25l_a$ (c) $\sigma_n = 0.35l_a$ (d) $\sigma_n = 0.5l_a$

Fig. 6: Shrinkage analysis during the denoising process. The Sphere model is corrupted with different levels of noise ($\sigma_n = 0.13l_a, 0.25l_a, 0.35l_a, 0.5l_a$) in random direction. An average of the L_2-norm of each vertex is computed to show a shrinkage effect in the proposed method. From Figure (a)-(d) the L_2-norms are 0.984, 0.983, 0.982 and 0.9811. Vertices are colored based on the variation of vertex normals. We computed the scalar product between the normal of a random vertex and rest of the vertex normals to show the level of denoising.

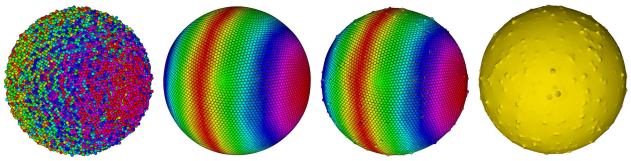

(a) $\sigma_n = 0.25l_a$ (b) $\varepsilon = 2l_a$ (c) $\varepsilon = l_a$ (d) $\varepsilon = l_a$, surface

Fig. 7: Effect of the distance-based constraint ε. Figure (a) shows a sphere, which is corrupted by Gaussian noise in random direction with standard deviation $\sigma_n = 0.25l_a$ and l_a is the average distance between vertices of the point set. Figure (b) represents a desirable noise-free output with $\varepsilon = 2l_a$ and when $\varepsilon = l_a$, the proposed method is not able to remove all noise components. The L_2-norms are 0.984 and 0.981 for Figure (b) and (c) respectively. Vertices are colored based on the variation of vertex normals. We computed the scalar product between the normal of a random vertex and rest of the vertex normals to show the level of denoising.

3.1. Parameters Tuning

We introduced several parameters: geometric neighbor radius r, dihedral angle threshold ρ (Equation (2)), eigenvalue threshold τ (Section 2.1.2), damping factor d (Equation (6)), distance-based constraint ε (Equations (11), (13), (14)), total number of iterations p, and vertex-diffusion speed α (Equation (14)). Throughout the whole experimentation, we fixed $\alpha = 0.1$ and $d = 3$. The radius r of the geometric neighborhood depends on the resolution of the input point set and it is fixed to be twice the average distance l_a between the vertices of the point set. The average distance between the vertices is computed using 6 nearest neighbors of each vertex. In this paper, we also fix the distance-based constraint $\varepsilon = 2r$ for the experimentation purpose (except Figure 7). Effectively, there are only 3 parameters (τ, ρ, p) to tune the results. In the quantitative comparison,

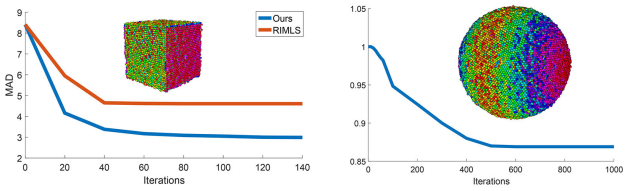

(a) MAD (b) E_v

Fig. 8: A visual representation of the convergence of the proposed algorithm. Figure (a) shows the orientation error convergence on a Cube model ($\sigma_n = 0.13l_a$) and Figure (b) demonstrates the L_2-norm variation with iterations on a noisy Sphere ($\sigma_n = 0.25l_a$).

see Table 1, the parameters are mentioned in the following format: (τ, ρ, p). For Methods [11], [12], and [30], we mention "Default" in the parameter column because the corresponding smooth models are provided by their authors. For the method [15], we used the parameters (h, #{*iterations*}, α), and for [16], we used (σ_r, σ_n), both listed in Table 1.

The eigenvalue threshold τ depends on the noise intensity on a point set. The bigger the noise intensity, the larger the value of τ should be chosen. We use $\tau \in \{0.25, \ldots, 0.4\}$ for synthetic data and $\tau \in \{0.05, \ldots, 0.1\}$ for real data because in our experiment real data point sets have smaller noise intensity compared to synthetic data point sets. We iterate several times ($p \in \{20, \ldots, 100\}$) for best results. The term $\rho \in \{0.8, \ldots, 0.95\}$ is the threshold to select the neighbor components and it is computed using the scalar product between the neighbor vertex normals. On a CAD model, we choose a high threshold value because of sharp features and on CAGD models, we choose a small threshold value because of smoother features compared to CAD models. The distance-based constraint ε is one of the most important parameter in the proposed algorithm. The effect of this parameter is shown in Figure 7. As it can be seen, a small value of ε leads to less shrinkage (small E_v) but does not remove all noise components.

3.2. Quantitative Analysis

We performed several experiments regarding the quantitative analysis of the proposed algorithm. In general, shrinkage and feature blurring are two main challenges during the denoising process. In this section, we show the behavior of the proposed algorithm against different levels of noise in terms of shrinkage and feature preservation.

To quantify shrinkage, we performed the denoising process with a unit Sphere and computed the L_2-norm of each vertex using the following equation:

$$E_v = \frac{1}{n}\sum_{i=0}^{n-1} \|\mathbf{v}_i\|^2. \tag{16}$$

For the original Sphere $E_v = 1.0$ and due to shrinkage effect the value of E_v decreases. As shown in Figure 6, the shrinkage effect increases with noise intensity but at the same time these changes are not significant. The value of E_v also depends on the distance-based constraint ε. As shown in Figure 7, with a bigger value of ε, it is possible that E_v will be bigger but at the same time it gives a smoother result compared to a small value of ε.

For further shrinkage analysis, we reconstructed triangulated surfaces using the "ball pivoting" algorithm [31] (Figure 9-12). To compute the closeness between the ground truth model and the denoised model, we use an L_2 vertex-based error metric, which is defined as in [32]:

$$D_v = \sqrt{\frac{1}{3\sum_{k\in F} a_k}\sum_{i\in V}\sum_{j\in F_v(i)} a_j \mathrm{dist}(\tilde{\mathbf{v}}_i, T)^2}$$

where F and V are treated as the triangular element set and the set of vertices respectively after the triangulated surface reconstruction. The terms a_k and a_j are the corresponding face areas. The distance $\mathrm{dist}(\tilde{\mathbf{v}}_i, T)$ is the closest L_2-distance between the newly computed vertex $\tilde{\mathbf{v}}_i$ and the triangle T of the reference model.

Table 1: Quantitative Comparison

Models	Methods	MAD	$D_v \times 10^{-3}$	Parameters
Cube $\lvert V\rvert$ = 1906 Figure 10	[15]	5.56	3.24	(2, 45, 0.5)
	[16]	4.62	5.41	(4, 0.75)
	[11]	4.60	3.37	Default
	[12]	3.48	7.51	Default
	[30]	4.47	6.46	Default
	Ours	**2.85**	**1.65**	(0.3, 0.95, 150)
Rocker arm $\lvert V\rvert$ = 24106 Figure 11	[15]	**5.13**	22.6	(4, 15, 0.5)
	[16]	5.26	**21.4**	(4, 1)
	[11]	6.31	33.0	Default
	[12]	8.14	118.7	Default
	[30]	6.26	72.12	Default
	Ours	7.56	43.26	(0.25, 0.9, 80)
Fan disk $\lvert V\rvert$ = 25894 Figure 9	[15]	**3.72**	1.7	(4, 15, 0)
	[16]	6.6	1.81	(4, 0.75)
	[11]	13.67	1.56	Default
	[12]	4.57	1.81	Default
	[30]	4.34	1.4	Default
	Ours	4.4	**1.39**	(0.3, 0.9, 150)
Octahedron $\lvert V\rvert$ = 40242 Figure 12	[15]	3.35	0.27	(2, 45, 0.5)
	[16]	4.31	0.39	(4, 0.75)
	[11]	4.6	0.32	Default
	[12]	1.2	0.52	Default
	[30]	1.37	0.49	Default
	Ours	**1.11**	**0.19**	(0.25, 0.9, 80)

To quantify feature preservation, we check the orientation error between the denoised model and the ground truth. Mean angular deviation (MAD) is defined to measure the orientation error:

$$MAD = \frac{1}{n}\sum_{i=0}^{n-1} \angle(\bar{\mathbf{n}}_i, \tilde{\mathbf{n}}_i), \tag{17}$$

where $\bar{\mathbf{n}}_i$ and $\tilde{\mathbf{n}}_i$ are vertex normals of the ground truth model and the denoised model respectively. Figure 5 shows that MAD is large when noise intensity is high. So with bigger noise, the orientation error will be bigger compared to lower noise. As it can be seen from Figure 5, for $\sigma_n = 0.13l_a$ to $\sigma_n = 0.35l_a$, the output models are noise-free with sharp features. However, with $\sigma_n = 0.5l_a$, we are not able to preserve all sharp features.

Table 1 shows the comparison of the proposed method with five state-of-the-art methods. As it can be seen, for the Cube

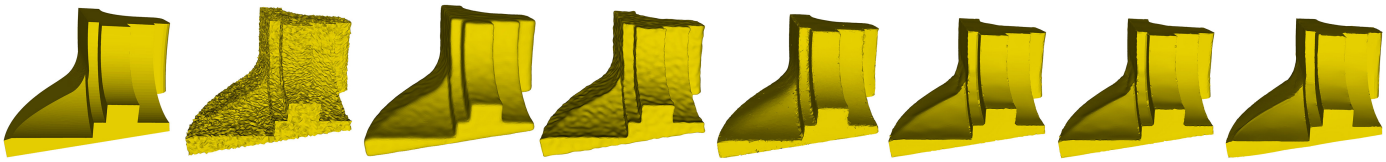

(a) Original (b) Noisy (c) APSS[15] (d) RIMLS [16] (e) MRPCA [11] (f) GN [12] (g) RN [30] (h) Ours

Fig. 9: The Fan disk model corrupted by Gaussian noise ($\sigma = 0.28l_e$), where l_e is the average distance between the vertices of the model. It can be seen that the proposed method is able to preserve sharp features effectively compared to state-of-the-art methods. Surfaces are reconstructed using the "ball pivoting" algorithm [31].

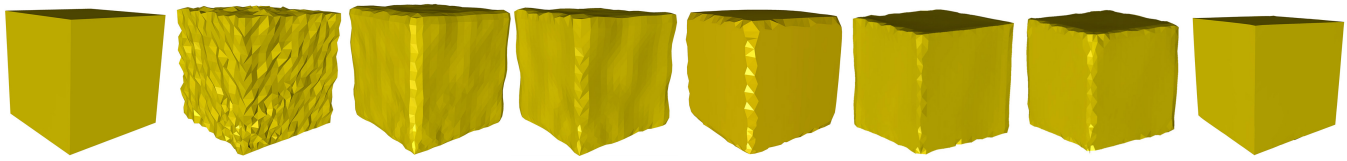

(a) Original (b) Noisy (c) APSS [15] (d) RIMLS [16] (e) MRPCA [11] (f) GN [12] (g) RN [30] (h) Ours

Fig. 10: The Cube model with non-uniform distribution of vertices, corrupted by Gaussian noise ($\sigma_n = 0.3l_e$), where l_e is the average distance between the vertices of the model. It can be seen that the proposed method is able to preserve sharp features effectively compared to state-of-the-art methods and does not create bumpy structures. Surfaces are reconstructed using the "ball pivoting" algorithm [31].

model, our method not only reconstructs sharp features (low MAD) but also produces minimum shrinkage (low D_v) compared to the current state-of-the-art methods. For the Rocker arm model, the proposed method is not as good as APSS [15] and RIMLS [16] methods in terms of MAD and D_v. However, Figure 11 shows that our method produces smoother umbilical regions with enhanced sharp features. For the Fan disk model, the proposed algorithm performs better compared to state-of-the-art methods in terms of feature preservation. However, it produces more volume shrinkage compared to APSS [15]. Similar to the Cube model, our algorithm outperforms state-of-the-art methods in terms of feature preservation and volume shrinkage.

Figure 8 shows the convergence property of the proposed algorithm. Figure 8(a) shows the orientation error with a noisy Cube model and it is almost constant after 100 iterations. As it can be seen from the figure, the proposed method has better convergence rate compared to RIMLS [16]. Our method has improved convergence rate because of the BEO (binary eigenvalues optimization), which assigns binary values to the eigenvalues of the vertex-based NVT. By assigning zero to the least dominant eigenvalue, our algorithm removes noise components faster compared to state-of-the-art methods. Similarly, Figure 8(b) shows the variation of E_v w.r.t. iterations. As the number of iterations increases, the value of E_v decreases, which leads to shrinkage effect. In the proposed method, the shrinkage effect is controlled using the distance-based constraint ε. As it can be seen from Figure 8, the value of E_v is almost constant after 400 iterations because the value of ε is set to approximately twice of the point set resolution.

3.3. Visual Comparison with State-of-the-art Methods

For visual comparison, we reconstruct triangulated meshes using the "ball pivoting" algorithm [31] after the point set denoising. Fan disk (Figure 9) and Cube (Figure 10) models have non-uniform vertices corrupted with Gaussian noise in random directions. Figure 10 shows that the proposed method produces a noise-free model with sharp features without creating any false and bumpy features like APSS [15] and RIMLS [16] methods. MRPCA [11], GN (guided normals) [12], and RN (rolling normals) [30] remove noise effectively from flat regions but edges and corners are not reconstructed properly. Similarly, Figure 9 shows that our method reconstructs not only sharp features, but also shallow features (around flat regions). APSS and RIMLS preserve different levels of features also but do not remove noise components effectively. MRPCA removes noise effectively but does not reconstruct shallow features. Visually, GN and RN produce an output which is quite similar to the proposed algorithm. However, our method produces better quantitative measures compared to GN and RN. The Rocker arm model (Figure 11) has a considerably non-uniform mesh and our method better enhances sharp features (around cylindrical regions) and removes noise more effectively compared to state-of-the-art methods. In terms of quantitative analysis, APSS (lowest MAD) and RIMLS (lowest D_v) are better compared to the proposed method. Figure 12 shows the capability of the proposed method to produce better corners and edges compared to MRPCA, APSS, and RIMLS and the results obtained by GN and RN methods look quite similar to the proposed method.

For real data, Figure 13 shows that our method removes noise effectively while retaining features on the surface compared to [15] and [16]. RN smooths out fine levels of features. GN and the proposed method produce quite similar results. Similarly, Figure 14 represents the applicability of the proposed method in medical data analysis. As it can be seen from the figure, our method removes noise effectively from the spherical regions and retains sharp features in the cylindrical regions. Guennebaud et al. [15] and Öztireli et al. [16] are not able to remove the noise components properly. MRPCA, GN, and RN remove noise components effectively. However, these methods

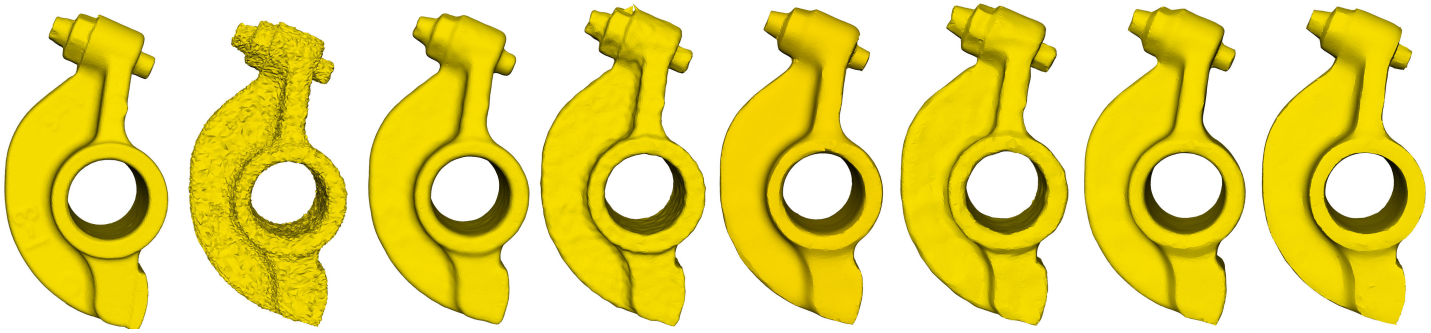

(a) Original (b) Noisy (c) APSS [15] (d) RIMLS [16] (e) MRPCA [11] (f) GN [12] (g) RN [30] (h) Ours

Fig. 11: The Rocker arm model corrupted by Gaussian noise (($\sigma_n = 0.3l_e$) in normal direction. The results are produced by state-of-the-art methods and our proposed method. The proposed method removes noise effectively and also enhances the sharp features around the cylindrical region. Surfaces are reconstructed using the "ball pivoting" algorithm [31].

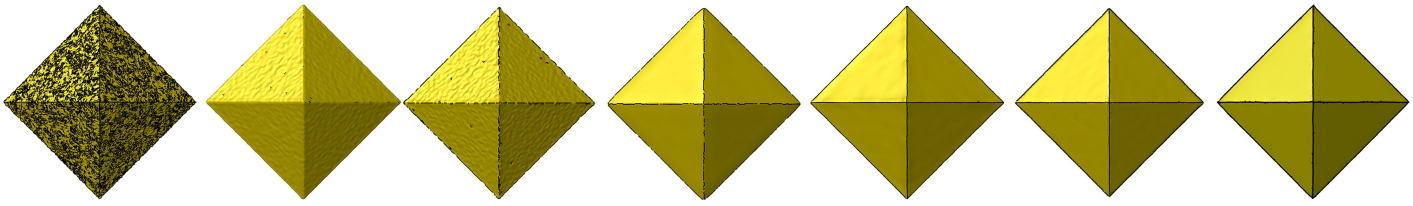

(a) Original (b) APSS [15] (c) RIMLS [16] (d) MRPCA [11] (e) GN [12] (f) RN [30] (g) Ours

Fig. 12: The Octahedron model, which is corrupted by Gaussian noise and results produced by the proposed method and state-of-the-art methods. Surfaces are reconstructed using the "ball pivoting" algorithm [31].

blur the sharp features in the cylindrical region.

Figure 15 shows the robustness of the proposed method against irregular sampling of data points. The Gargoyle model is scanned by a laser scanner and has a highly irregular sampling. As it can be seen from the figure, our method produces a noise-free point set of the Gargoyle model without blurring different levels of features.

4. Conclusion

In this paper, we presented a simple and effective tensor multiplication algorithm for feature-preserving point set denoising. The proposed method is basically an extension of the ENVT-based mesh denoising [5]. Similar to the concept of the ENVT, in the proposed algorithm, we used vertex-based NVT and the spectral analysis of this tensor leads to decoupling of features from noise. Noise components are removed by the multiplication of the vertex-based NVT to the corresponding vertex normal. The concept of binary eigenvalues optimization not only enhances sharp features but also improves the convergence rate of the method. Local binary neighborhood selection helps to select similar vertices in the neighborhood to compute the vertex-based NVT to avoid feature blurring during the denoising process. After the vertex normal filtering, we classify feature points into edges, corners and flat regions using an anisotropic covariance matrix. For the vertex update stage, we introduced restricted least square error metrics, which are different for different kinds of features. The vertex position reconstruction using restricted quadratic error metrics helps the algorithm to recreate the sharp edges and corners. The experimental results show the effectiveness of the proposed algorithm.

Our method is capable of handling noise, but yields erroneous results under high noise intensities. This is based on the fact, that noise has a great impact on the normal estimation and the NVT construction, and we use them throughout the whole process. Another issue arises when the input point set is highly irregular. As we have shown in Figure 15, our method is robust up to a moderate level of irregularity but it is possible that with extreme irregular sampling, the output may not be satisfactory.

During the denoising process, we tuned the different parameters manually to get the desired results. we need to find an optimal combination of the parameters automatically. A direction we are going to investigate in the future.

Acknowledgments

This research was supported by the DFG Collaborative Research Center TRR 109, "Discretization in Geometry and Dynamics".

(a) Original (b) APSS [15] (c) RIMLS [16] (d) MRPCA [11] (e) GN [12] (f) RN [30] (g) Ours

Fig. 13: Real data of the Rabbit model, acquired by a 3D scanner and results produced by the proposed method and state-of-the-art methods. Surfaces are reconstructed using the "ball pivoting" algorithm [31].

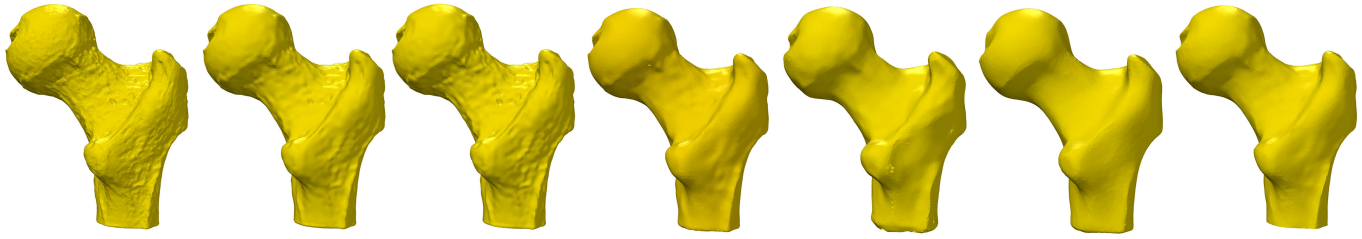

(a) Original (b) APSS[15] (c) RIMLS [16] (d) MRPCA [11] (e) GN [12] (f) RN [30] (g) Ours

Fig. 14: The Ball joint model – which is corrupted by scanner noise – and results produced by the proposed method and state-of-the-art methods. Surfaces are reconstructed using the "ball pivoting" algorithm [31].

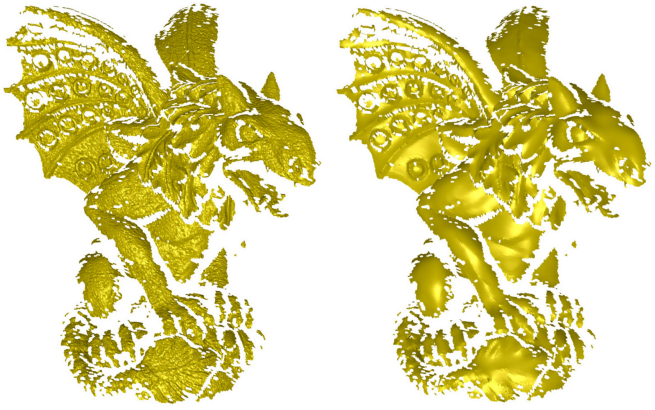

(a) Noisy irregular real data (b) Our result

Fig. 15: Robustness against irregular data points. Figure (a) shows the noisy irregular data points of the Gargoyle model and Figure (b) shows the result obtained by the proposed method.

References

[1] Levoy, M, Whitted, T. The use of points as a display primitive. University of North Carolina, Department of Computer Science; 1985.

[2] Boehnen, C, Flynn, P. Accuracy of 3d scanning technologies in a face scanning scenario. In: IEEE Fifth International Conference on 3D Digital Imaging and Modeling. 2005, p. 310–317.

[3] Buck, U, Naether, S, Braun, M, Bolliger, S, Friederich, H, Jackowski, C, et al. Application of 3d documentation and geometric reconstruction methods in traffic accident analysis with high resolution surface scanning, radiological msct/mri scanning and real data based animation. Forensic science international 2007;170(1):20–28.

[4] Levoy, M, Pulli, K, Curless, B, Rusinkiewicz, S, Koller, D, Pereira, L, et al. The digital michelangelo project: 3d scanning of large statues. In: Proceedings of the 27th annual conference on Computer graphics and interactive techniques. 2000, p. 131–144.

[5] Yadav, SK, Reitebuch, U, Polthier, K. Mesh denoising based on normal voting tensor and binary optimization. IEEE Transactions on Visualization and Computer Graphics 2017;PP(99):1–1. doi:10.1109/TVCG.2017.2740384.

[6] Amenta, N, Kil, YJ. Defining point-set surfaces. ACM Trans Graph 2004;23(3):264–270. URL: http://doi.acm.org/10.1145/1015706.1015713. doi:10.1145/1015706.1015713.

[7] Mitra, NJ, Nguyen, A. Estimating surface normals in noisy point cloud data. In: Proceedings of the Nineteenth Annual Symposium on Computational Geometry. ACM; 2003, p. 322–328. URL: http://doi.acm.org/10.1145/777792.777840. doi:10.1145/777792.777840.

[8] Fleishman, S, Drori, I, Cohen-Or, D. Bilateral mesh denoising. ACM Trans Graph 2003;22(3):950–953. URL: http://doi.acm.org/10.1145/882262.882368. doi:10.1145/882262.882368.

[9] Lange, C, Polthier, K. Computer Aided Geometric Design. Computer Aided Design 2005;22:680–692.

[10] Sun, Y, Schaefer, S, Wang, W. Denoising point sets via l_0 minimization. Comput Aided Geom Des 2015;35:2–15. URL: http://dx.doi.org/10.1016/j.cagd.2015.03.011. doi:10.1016/j.cagd.2015.03.011.

[11] E., M, A., C. Point cloud denoising via moving rpca. Computer Graphics Forum 2016;36(8):123–137. URL: https://onlinelibrary.wiley.com/doi/abs/10.1111/cgf.13068. doi:10.1111/cgf.13068.

[12] Zheng, Y, Li, G, Wu, S, Liu, Y, Gao, Y. Guided point cloud denoising via sharp feature skeletons. Vis Comput 2017;33(6-8):857–867. URL: https://doi.org/10.1007/s00371-017-1391-8. doi:10.1007/s00371-017-1391-8.

[13] Berger, M, Tagliasacchi, A, Seversky, LM, Alliez, P, Guennebaud, G, Levine, JA, et al. A survey of surface reconstruction from point clouds. Comput Graph Forum 2017;36(1):301–329. URL: https://doi.org/10.1111/cgf.12802. doi:10.1111/cgf.12802.

[14] Levin, D. Mesh-independent surface interpolation. In: Geometric Modeling for Scientific Visualization; vol. 3. 2003, p. 37–49.

[15] Guennebaud, G, Gross, M. Algebraic point set surfaces. ACM Trans Graph 2007;26(3). URL: http://doi.acm.org/10.1145/1276377.1276406. doi:10.1145/1276377.1276406.

[16] Oztireli, C, Guennebaud, G, Gross, M. Feature preserving point set surfaces based on non-linear kernel regression. Computer Graphics Forum 2009;28(2):493–501.

[17] Chen, J, Guennebaud, G, Barla, P, Granier, X. Non-oriented mls gradient fields. Computer Graphics Forum 2013;32(8):98–109. URL: http://dx.doi.org/10.1111/cgf.12164. doi:10.1111/cgf.12164.

[18] Ohtake, Y, Belyaev, A, Alexa, M, Turk, G, Seidel,

HP. Multi-level partition of unity implicits. ACM Trans Graph 2003;22(3):463–470. URL: http://doi.acm.org/10.1145/882262.882293. doi:10.1145/882262.882293.

[19] Fleishman, S, Cohen-Or, D, Silva, CT. Robust moving least-squares fitting with sharp features. ACM Trans Graph 2005;24(3):544–552. URL: http://doi.acm.org/10.1145/1073204.1073227. doi:10.1145/1073204.1073227.

[20] Wang, J, Yu, Z, Zhu, W, Cao, J. Feature-preserving surface reconstruction from unoriented, noisy point data. Computer Graphics Forum 2013;32(1):164–176. URL: http://dx.doi.org/10.1111/cgf.12006. doi:10.1111/cgf.12006.

[21] Avron, H, Sharf, A, Greif, C, Cohen-Or, D. l_1-sparse reconstruction of sharp point set surfaces. ACM Trans Graph 2010;29(5):135:1–135:12. URL: http://doi.acm.org/10.1145/1857907.1857911. doi:10.1145/1857907.1857911.

[22] Huang, H, Wu, S, Gong, M, Cohen-Or, D, Ascher, U, Zhang, HR. Edge-aware point set resampling. ACM Trans Graph 2013;32(1):9:1–9:12. URL: http://doi.acm.org/10.1145/2421636.2421645. doi:10.1145/2421636.2421645.

[23] Lipman, Y, Cohen-Or, D, Levin, D, Tal-Ezer, H. Parameterization-free projection for geometry reconstruction. ACM Trans Graph 2007;26(3). URL: http://doi.acm.org/10.1145/1276377.1276405. doi:10.1145/1276377.1276405.

[24] Hoppe, H, DeRose, T, Duchamp, T, McDonald, J, Stuetzle, W. Surface reconstruction from unorganized points. SIGGRAPH Comput Graph 1992;26(2):71–78. URL: http://doi.acm.org/10.1145/142920.134011. doi:10.1145/142920.134011.

[25] Yadav, SK, Reitebuch, U, Polthier, K. Robust and high fidelity mesh denoising. IEEE Transactions on Visualization and Computer Graphics 2018;:1–1doi:10.1109/TVCG.2018.2828818.

[26] Medioni, G. Tensor voting: Theory and applications. 2000.

[27] Garland, M, Heckbert, PS. Surface simplification using quadric error metrics. In: Proceedings of the 24th annual conference on Computer graphics and interactive techniques. 1997, p. 209–216.

[28] Sun, X, Rosin, P, Martin, R, Langbein, F. Fast and effective feature-preserving mesh denoising. IEEE transactions on visualization and computer graphics 2007;13(5).

[29] Zheng, Y, Li, G, Wu, S, Liu, Y, Gao, Y. Guided point cloud denoising via sharp feature skeletons. The Visual Computer 2017;33(6-8):857–867.

[30] Zheng, Y, Li, G, Xu, X, Wu, S, Nie, Y. Rolling normal filtering for point clouds. Computer Aided Geometric Design 2018;URL: http://www.sciencedirect.com/science/article/pii/S0167839618300189. doi:https://doi.org/10.1016/j.cagd.2018.03.004.

[31] Bernardini, F, Mittleman, J, Rushmeier, H, Silva, C, Taubin, G. The ball-pivoting algorithm for surface reconstruction. IEEE Transactions on Visualization and Computer Graphics 1999;5(4):349–359. doi:10.1109/2945.817351.

[32] Sun, X, Rosin, P, Martin, R, Langbein, F. Fast and effective feature-preserving mesh denoising. Visualization and Computer Graphics, IEEE Transactions on 2007;13(5):925–938.